



HAL
open science

Scale selection in columnar jointing: Insights from experiments on cooling stearic acid and numerical simulations

Amalie Christensen, Christophe Raufaste, Marek Misztal, Franck Celestini, Maria Guidi, Clive Ellegaard, Joachim Mathiesen

► To cite this version:

Amalie Christensen, Christophe Raufaste, Marek Misztal, Franck Celestini, Maria Guidi, et al.. Scale selection in columnar jointing: Insights from experiments on cooling stearic acid and numerical simulations. *Journal of Geophysical Research: Solid Earth*, 2016, 121 (3), pp.1462-1482. 10.1002/2015JB012465 . hal-01358085

HAL Id: hal-01358085

<https://hal.science/hal-01358085>

Submitted on 6 Feb 2022

HAL is a multi-disciplinary open access archive for the deposit and dissemination of scientific research documents, whether they are published or not. The documents may come from teaching and research institutions in France or abroad, or from public or private research centers.

L'archive ouverte pluridisciplinaire **HAL**, est destinée au dépôt et à la diffusion de documents scientifiques de niveau recherche, publiés ou non, émanant des établissements d'enseignement et de recherche français ou étrangers, des laboratoires publics ou privés.

1 **Scale selection in columnar jointing: insights from**
2 **experiments on cooling stearic acid and numerical**
3 **simulations**

Amalie Christensen,¹ Christophe Raufaste,² Marek Misztal,¹ Franck

Celestini,² Maria Guidi,¹ Clive Ellegaard¹ and Joachim Mathiesen^{1,2}

- 4 • Scale selection in columnar jointing is a nontrivial function of material properties and cooling
5 conditions
- 6 • Columnar jointing is reproduced experimentally in a model system using cooling stearic acid
- 7 • Proposed model can be used in the prediction of the cooling rate of columnar jointed systems

¹Niels Bohr Institute, University of
Copenhagen, Blegdamsvej 17, DK-2100
Copenhagen, Denmark

²Université Nice Sophia Antipolis, CNRS,
LPMC, UMR 7336, Parc Valrose, 06100
Nice, France

8 **Abstract.** Many natural fracture systems are characterized by a single
9 length scale, which is the distance between neighboring fractures. Examples
10 are mudcracks and columnar jointing. In columnar jointing the origin of this
11 scale has been a long-standing issue. Here we present a comprehensive study
12 of columnar jointing based on experiments on cooling stearic acids, numer-
13 ical simulations using both discrete and finite element methods and basic an-
14 alytical calculations. We show that the diameter of columnar joints is a non-
15 trivial function of the material properties and the cooling conditions of the
16 system. We determine the shape of this function analytically and show that
17 it is in agreement with the experiments and the numerical simulations.

1. Introduction

18 Spectacular geometric patterns, such as Giant's Causeway at the Irish shoreline, Devil's
19 Tower in Wyoming or Svartifoss in Iceland (Figure 1a), are examples of columnar joint-
20 ing in igneous rocks. Several hypotheses for the physical process resulting in columnar
21 jointing have historically been proposed, such as the columns being crystals of quartz or
22 the columns being regular packings of spherulites [Tomkeieff, 1940]. It is now widely
23 accepted that columnar jointing in igneous rock is a result of thermal contraction, an
24 idea developed in the late 19th century [Mallet, 1875]. As the igneous body cools it con-
25 tracts. If the contraction is uniform, no stress will be generated in the rock, whereas a
26 non-uniform contraction, e.g. due to temperature gradients, will generate stress. Above
27 the glass transition temperature of the rock, T_G , the stress is viscously dissipated, but
28 below T_G stress starts to accumulate. When the stress exceeds the fracture threshold,
29 the accumulated elastic energy is transformed to surface energy by fractures. As the rock
30 further cools with time, the T_G isotherm propagates toward the interior of the rock and
31 with it the fracture front. In that way a network of fractures, or so-called joints, is created
32 and it divides the rock into columns.

33 Igneous columnar jointing occurs in lava flows, lava lakes, sills, dikes and ash-flow tuffs
34 [Hetényi et al., 2012; Spry, 1962]. The columns are commonly polygonal shaped, with
35 the diameter being approximately constant over a significant fraction of their height. The
36 observed diameters range from a few cm up to 3m while the column height can be up
37 to 30m. The regular columns tend to have 5, 6 or 7 sides, although 3-, 4-, and 8-sided
38 columns exist as well [Hetényi et al., 2012; Phillips et al., 2013; Spry, 1962]. As illustrated

39 in Figure 1b, the regular columns can be intersected by a highly disorganized region
 40 with smaller curvy columns. The two types of regions are commonly termed colonnade
 41 and entablature, respectively [Tomkeieff, 1940]. Figure 1c illustrates striations on the
 42 surface of columnar joints. The striations are linear bands oriented perpendicular to the
 43 crack propagation direction and are produced by stepwise crack advance, where the crack
 44 advance length corresponds to the striae height, s [Ryan and Sammis, 1981].

45 Under certain conditions, columnar jointing can be reproduced at the lab scale in des-
 46 iccating starch slurries [Goehring *et al.*, 2015, 2006; Müller, 1998, 2001; Toramaru and
 47 Matsumoto, 2004]. In general, desiccation cracks differ from columnar jointing, since the
 48 contraction of the desiccating substance, e.g. mud, is limited to the surface in contact
 49 with air. The cracks therefore have a short penetration depth [Groisman and Kaplan,
 50 1994]. In contrast to columnar jointing, mud cracks typically have a hierarchical struc-
 51 ture, where domains bounded by existing cracks are divided by secondary cracks meeting
 52 existing cracks at 90 degree angles [Bohn *et al.*, 2005]. Hierarchical fracture patterns are
 53 also produced by serpentinization processes in e.g. dyke-host complexes [Iyer *et al.*, 2008]
 54 and by weathering processes [Røyne *et al.*, 2008]. Common for most hierarchical fracture
 55 patterns is the lack of a maturation process similar to that observed in cooling basalt,
 56 where the fracture network has time to mature as it propagates with the cooling front
 57 [Hofmann *et al.*, 2015].

The internal stress generated by the contraction of a material, $\beta = \alpha_T \Delta T$, will in a linear elastic approximation be proportional to $E\beta/(1 - 2\nu)$, where E is the Young modulus, α_T the coefficient of linear thermal expansion, ΔT a temperature change and ν the Poisson ratio. The stress generation will be lower if the material contraction changes from 0 to

β over a length scale w and in the limit of large w , the stress becomes vanishingly small. Inspired by desiccating thin films and mud, we write the magnitude of the internal stress σ in terms of a scaling function f :

$$\sigma = E\beta f(w, \nu, \dots) \quad (1)$$

58 The internal stress is dependent on material properties, such as Young's modulus E ,
 59 Poisson's ratio ν and coefficient of linear thermal expansion α_T , as well as on the externally
 60 imposed cooling conditions determined by the temperature change ΔT and the length scale
 61 w . The internal stress might depend on further material properties such as the thermal
 62 diffusivity D , the fracture toughness $K_{I,c}$ or cooling conditions.

63 Asymptotic shapes of such a scaling function has been suggested in [*Hayakawa, 1994*].
 64 For desiccation in thin film systems, the scaling function can be estimated analytically
 65 [*Cohen et al., 2009*]. Here, we will determine the shape and dependencies of the scaling
 66 function, f , for columnar jointing from simple analytical models and from numerical
 67 simulations and compare with experiments on cooling stearic acid.

1.1. Heat extraction mechanism

68 The stress accumulation in a cooling igneous body is controlled by the magnitude of
 69 the temperature gradients, which again is controlled by the heat transport in the mate-
 70 rial. Two main modes of heat transport during columnar jointing have been considered
 71 in the literature, bulk heat conduction and crack aided convective cooling, respectively.
 72 In general, conductive cooling leads to a temperature profile flattening as time progresses
 73 and therefore results in an increase of column diameters with time. In contrast, convec-
 74 tive cooling can maintain a steep temperature profile and therefore also a fixed column

75 diameter. Below we shall focus on the convective cooling mode and only briefly discuss
76 the conductive mode.

77 1.1.1. Conductive cooling

As a simple model, one can consider the igneous body as a homogeneous and isotropic half space $X \geq 0$ where we imagine the X -axis to point into the igneous body. Due to the assumed homogeneity and infinite extent of the Y - and Z -dimensions, the temperature field is only a function of X . For pure bulk heat diffusion the temperature field is governed by:

$$\frac{\partial T(X, t)}{\partial t} = D \nabla^2 T(X, t) \quad (2)$$

At the interface, $X = 0$, the igneous body is in contact with a cooling surface which we assume efficiently removes heat, such that the temperature of this surface is always T_0 , i.e. $T(X = 0, t) = T_0$. The initial temperature of the body at $t = 0$ is taken to be homogeneously T_1 , i.e. $T(X > 0, t = 0) = T_1$. If we do not consider latent heat, the present boundary conditions yield:

$$T(X, t) = T_0 + (T_1 - T_0) \operatorname{erf}\left(\frac{X}{2\sqrt{Dt}}\right) \quad (3)$$

78 where the error function is defined as: $\operatorname{erf}(\eta) = \frac{2}{\sqrt{\pi}} \int_0^\eta e^{-\tau^2} d\tau$. If we assume that the
79 igneous body can be described as a linear elastic material (infinite in the Y - and Z -
80 dimensions), then from Eq. (3), we see that the only natural length scale in the system
81 must be proportional to \sqrt{Dt} . We would therefore expect the stria height as well as the
82 average column diameter to increase with the square root of time, or equivalently, the
83 distance from the cooling surface. Here, we have neglected the latent heat, but the result
84 from including latent heat is qualitatively identical. The profile again flattens proportional
85 to the square root of time. While an increase in striae height has been observed within a

86 few meters from the cooling surfaces [*Ryan and Sammis, 1978; Degraff and Aydin, 1993*],
 87 jointed igneous rock commonly has a constant striae height over much of the column
 88 height [*Goehring and Morris, 2008; Phillips et al., 2013*]. The constant stria height could
 89 be explained if the system had one fixed length scale. A fixed length scale is a possibility
 90 in convective cooled systems.

91 1.1.2. Convective cooling

Borehole temperature measurements of the Kilauea Iki lava lake [*Hardee, 1980*] showed a constant temperature of 100°C in the upper part of the solidified basalt. This suggests, that the mechanism responsible for stabilizing the heat extraction rate and thereby the speed of the temperature profile is convection of water/steam in the joints. We shall therefore assume that the water and steam zone propagates through the cooling body at a constant velocity $\mathbf{v} = v\hat{\mathbf{X}}$ and that the entire convection zone is at temperature $T_0 = 100^{\circ}\text{C}$. The water and steam convection results in a moving boundary condition of $T(X, t) = T_0$ at the position $X - vt = 0$ for the heat diffusion equation in Eq. (2). To implement this boundary condition, we change the reference to a frame moving with the convection zone and rescale by a characteristic length, ℓ , of the system, $x = (X - vt)/\ell$. In steady state, the heat diffusion equation in the moving frame reduces to:

$$\frac{1}{Pe} \frac{\partial^2 T}{\partial x^2} + \frac{\partial T}{\partial x} = 0, \quad (4)$$

where we have introduced the Péclet number $Pe = v\ell/D$ which is the ratio of the heat advection and heat diffusion rates. The Péclet number can also be thought of as the ratio, $Pe = \ell/w$, between the column diameter ℓ and the width of the thermal front $w = D/v$.

The general solution to Eq. (4) is:

$$T(x) = \Delta T (1 - e^{-Pe x}) \theta(x) + T_0, \quad (5)$$

92 where $\theta(x)$ is the Heaviside step function, $\Delta T = T_1 - T_0$ and T_0, T_1 are the temperatures
 93 at $x = 0$ and $x = \infty$ respectively. T_0 is the temperature of the convection zone and
 94 T_1 is the emplacement temperature. This temperature profile is similar to the profile
 95 employed by [Hardee, 1980] which yielded good agreement with borehole measurements
 96 at the Kilauea Iki lava lake. Eq. (5) has a fixed shape in the frame of reference moving with
 97 the convection zone and is therefore expected to result in columnar joints with constant
 98 diameter, ℓ , and constant striae height, s .

1.2. Scaling of the column diameter

99 Basalt columns typically have a constant column diameter over most of their height
 100 [Peck and Minakami, 1968; Goehring and Morris, 2008; Phillips et al., 2013]. The speed
 101 of the temperature front, which is proportional to the cooling rate, is widely considered
 102 the governing quantity of the column diameter [Budkewitsch, 1994; Grossenbacher and
 103 McDuffie, 1995], with faster cooling leading to slenderer columns. As Budkewitsch [1994]
 104 notes, the rate of heat extraction from a convectional cooled igneous body is equal to the
 105 heat transferred from the hot interior to the crack network. Assuming that 1 m of crack in
 106 the plane perpendicular to the column axes can only transport a certain amount of heat,
 107 the length of the crack network in this plane would have to increase with increased cooling
 108 rate, i.e the column diameter would decrease. Based on data from desiccating starch
 109 experiments and the igneous columnar joints at the Island of Staffa and the Columbia
 110 River Basalt Group, it was observed that the column diameter, ℓ , correlates with the

111 inverse of the temperature front speed, $1/v$ [Goehring *et al.*, 2009]. From the definition of
112 the Péclet number, it was proposed that igneous columnar jointing proceeds at a constant
113 Péclet number of $Pe = 0.3 \pm 0.2$.

114 *Hetényi et al.* [2012] further found, that the geological setting (lava flow, lava lake, lava
115 dome, sill, dyke) exerted control on the columnar diameter, through control of the surfaces
116 where heat can be exchanged with the environment and thereby the cooling rate. When
117 the bodies were geometrically unconstrained (lava flows), they found chemistry to play
118 a role, through its control of material properties and through its control of emplacement
119 geometry, which in turn affects the cooling rate.

120 Though thermal contraction is widely believed to be the mechanism governing the
121 column formation process, other models where fingering in the solidifying lava governs
122 the column scale, such as large scale constitutional supercooling [Guy, 2010; Gilman,
123 2009] or double-diffusive convection [Kantha, 1981], have been proposed. These models
124 were not found consistent with a small-scale study of a single basalt column [Bosshard
125 *et al.*, 2012], and do not fully explain the striking similarity between columnar jointing in
126 basalt and corn starch.

127 All the above considerations assume a one-to-one relation between material properties,
128 cooling parameters and the resulting column diameter. Alternatively, one might imagine
129 that there is a range of possible column diameters for each set of material properties and
130 cooling parameters. Goehring *et al.* [2006] found in desiccating corn starch experiments,
131 that for the same initial evaporation rate there existed a column diameter stable over a
132 range of final evaporation rates. Jagla and Rojo [2002] numerically studied the evolution
133 of a parallel array of cracks in a directionally dried system. They found that the distance

134 between the parallel cracks was governed by the typical length scale at the surface where
135 cooling was initiated. In contrast to this finding, *Bahr et al.* [2009] deduced from a
136 numerical bifurcation analysis in three dimensions, the existence of a smallest possible
137 column diameter for each value of the crack front propagation velocity.

138 For columnar jointed igneous rock, there is to our knowledge no clear evidence of a one-
139 to-one relation between material properties (such as $E, \alpha_T, D, K_{I,c}$), cooling parameters
140 (such as $\Delta T, w$) and the column diameter. Though the studies of column diameter versus
141 geological emplacement and column diameter versus cooling rate show correlations, none
142 of these data sets are strong enough to imply a one-to-one relationship. We will therefore
143 explore the idea of a range of possible columns diameters.

1.3. Organization of the article

144 In this article, we shall investigate the scaling of columnar joints through three-
145 dimensional numerical simulations, available field data and a new experimental system
146 based on the cooling of stearic acid. The stearic acid experiments are presented in Sec-
147 tion 2. A simple two-dimensional model for columnar jointing is introduced in Section
148 3, and the idea of a range of possible columns diameters for each system configuration
149 is explored analytically and numerically in Section 4. We use the numerical simulations
150 and analytical arguments to derive a quantitative relation between the Péclet number and
151 material properties and cooling conditions. While the analytical arguments follow from
152 two-dimensional considerations, we show from numerical simulations that the arguments
153 are also valid in three dimensions. Finally, we compare our findings with experiments
154 on cooling stearic acid and field observations on igneous columnar jointing. Concluding
155 remarks are offered in Section 5.

2. Experiments on cooling stearic acid

156 We propose stearic acid as a new model system for columnar jointing. As opposed to
157 the widely studied corn starch model system, columnar jointing in stearic acid is driven
158 by thermal contraction and not by desiccation.

159 Experiments were performed on stearic acid (a fatty acid of chemical formula $C_{18}H_{36}O_2$).
160 It is a waxy solid at room temperature with a solidification temperature $T_S = 69.3^\circ\text{C}$.
161 The products are provided by VWR Chemicals (technical grade) and contains a minimum
162 of 90% of stearic and palmitic acids.

163 Initially, the wax is melted and brought to a temperature of $T_1 = 120^\circ\text{C}$. The liquid
164 is poured inside a cylindrical aluminum can that is placed inside a coolant liquid, liquid
165 nitrogen at $T_0 = -196^\circ\text{C}$, and solidification occurs from the can edges towards the bulk
166 of the sample. At the end of the solidification process, the sample is broken into pieces to
167 image the inner structure. A columnar structure appears inside the solid stearic acid at
168 the contact with the aluminum can and extends roughly 2 cm inwards (Figure 2a). On
169 the rest of the sample, no organized structure is observed. At the end of the experiment,
170 the sample exhibits a volume decrease of approximately 10%.

171 Post-solidified samples are imaged in depth by X-ray microtomography (Figure 2c-2f).
172 The scanner is a SkyScan1172, with a source voltage of 59 kV and a source current of
173 $167 \mu\text{A}$. The stearic acid samples have a surface of order $15 \times 15 \text{ mm}^2$ and a depth of
174 about 20 mm. The average area of the columns is analyzed and plotted as a function
175 of the depth from the cooling surface in Figure 2b. We find that the column area is
176 rather constant through the jointed region though an increasing trend might be present.

177 Assuming perfect hexagonal columns, the average column area is used to estimate the
178 column diameter, $\ell = (2 \pm 1)$ mm.

179 The solidification front velocity is estimated by stopping the solidification of similar
180 samples at different times (liquid stearic acid is removed from the can in less than 2s) and
181 measuring a posteriori the solid thickness. We find that the velocity is rather constant
182 with a typical solidification front velocity of $5 \mu\text{m/s}$.

183 In situ measurements are performed as well by immersing an array of thermocouples
184 (0.4 mm between each of them spanning 5.6 mm in total) inside the liquid stearic acid.
185 The thermocouple measurements confirm the constant solidification front velocity found
186 previously and give indications about the temperature profile. The temperature profile
187 is flattening with time because the width of the temperature front, w , is increasing, but
188 also because the temperature difference, $\Delta T = T_1 - T_0$, between the melt and the coolant
189 liquid is slightly decreasing. In fact, the emplacement temperature, T_1 , is decreasing in the
190 experiment from its initial value to the solidification temperature, T_S , and consequently
191 ΔT is varying over 15%. This variation is rather small, and does not significantly affect
192 the temperature profile predicted by the conductive cooling model, Eq. (3), but seems
193 to be enough to affect the front velocity. While the flattening of the temperature profile
194 should induce a front velocity decrease, the fact that T_1 approaches T_S as the experiment
195 proceeds seems to counteract the former effect and maintain a constant solidification front
196 velocity. The value of the temperature front width, w , is determined as the width over
197 which the temperature changes from the coolant temperature, T_0 , to the solidification
198 temperature, T_S . The value of w increases with time and we estimate its range of values
199 as $w = (4 \pm 2)$ mm for our thermocouple measurements. The experimental values for

200 the average column diameter and front width are used to estimate a Péclet number of
201 $Pe = \ell/w = 0.5 \pm 0.4$ for the stearic acid system.

202 We interpret the termination of the columnar joints after 2 cm to be caused by the
203 flattening of the temperature profile, such that the temperature gradient falls below a
204 threshold needed for fracturing to occur. We noted the presence of columns with other
205 coolant liquids. Using water at 0°C, we could observe a columnar structure with about the
206 same column diameter but the columns extended only a few millimeters into the sample.
207 For the water-cooled samples, the temperature difference, $T_1 - T_0$, is about one third of
208 the temperature difference obtained with nitrogen as coolant. The temperature gradient
209 therefore decreases below the threshold value necessary for fracture to occur faster than
210 in the nitrogen cooled case and the columns do not extend as far into the sample.

211 We noticed that purer samples of stearic acid led to the formation of crystalline struc-
212 tures spreading through the whole sample while it solidified and cooled down. In this case,
213 no columnar structure was observed. Addition of palmitic acid (5-50% in mass), as found
214 in the technical grade, leads to the formation of columns but with a smaller diameter, a
215 better cohesion and with a shiny aspect suggesting the presence of larger crystals. The
216 presence of impurities in the technical grade might prevent the formation of larger crystal
217 structures.

218 Tensile loading measurements were performed on cylindrical samples (5 mm in diameter,
219 5 cm in height) prepared as follows: after the wax is melted, we let the liquid stearic acid
220 cool down and solidify slowly at room temperature to prevent the formation of columnar
221 structures. At room temperature, the tensile strength is $\sigma_c = (0.34 \pm 0.06)$ MPa and the
222 Young modulus $E = (410 \pm 50)$ MPa.

223 If a better control of the temperature evolution is gained, we suggest that the stearic
224 acid experiments can be used as a model system for igneous columnar jointing in order to
225 gain insight into the effect of an initial surface crack pattern, to study if two crack fronts
226 approaching each other can produce an entablature like region and to study the effect of
227 the confining geometry. Also the possibility of a range of possible column diameters for
228 each set of material properties and cooling parameters could be investigated. Since we do
229 not yet have the required control of the temperature evolution, the models developed in
230 this paper will instead mainly be compared to numerical simulations and available field
231 measurements for basalt.

3. A two-dimensional model of columnar jointing

232 To model the idea of a range of possible column diameters, we consider the idealized
233 version of a system undergoing columnar jointing shown in Figure 3a. We will further
234 simplify the model to an array of semi-infinite cracks in a two-dimensional linear-elastic
235 strip as displayed in Figure 3b. The two-dimensional strip can be thought of as resulting
236 from a plane cut along the red dashed line in Figure 3a. Due to the symmetry of the
237 system, the same plane cut will be encountered repeatedly with a distance of approxi-
238 mately 2ℓ as one moves in the perpendicular Z -direction. We thus expect the Z -direction
239 to be of less importance than the X and Y -directions. Real columnar joint formations are
240 neither two-dimensional, nor perfectly hexagonal, and the validity of the two-dimensional
241 model thus ultimately relies on the agreement between the three-dimensional numerical
242 simulations presented in Section 4 and the predictions of the two-dimensional model.

The two-dimensional strip is displayed in Figure 3b together with a temperature profile,
 $T_{w,a}(X)$, of the Eq. (5) type, which is expected to lead to columnar jointing with a constant

diameter, ℓ . This temperature profile has a fixed shape in a frame of reference moving with the convection zone at speed v as discussed in Section 1.1.2. In contrast to previous sections, we now take the coordinate system (X, Y, Z) to be the frame of reference moving with the convection zone and the crack tips, with the crack tips located at $Z = 0$. For the purpose of calculating thermal contraction, we are only interested in the temperature deviation from the un-contracted molten interior at infinity and we therefore consider:

$$T_{w,a}(X) = \Delta T (1 - e^{-(X+a)/w}) \theta(X+a) - \Delta T \quad (6)$$

243 where $\Delta T = T_1 - T_0$ is the maximal temperature difference with respect to the temperature
 244 of the undeformed system, a is the signed distance between the temperature front and the
 245 crack tips and the length scale, w , describes the width of the temperature profile. T_1 is
 246 taken to be the emplacement temperature of the lava and $T_0 = 100^\circ C$ is the temperature
 247 of the steam filled cracks. For columnar jointing in igneous rock, only $a > 0$ is relevant,
 248 since the case $a < 0$ would imply that the steam/water convection zone penetrates further
 249 into the rock than the cracks. We will therefore refer to a as the crack lead length.

In dimensionless form, the temperature field in Eq. (6) in the moving frame of reference become:

$$T_{Pe,\delta}(x) = \frac{T_{w,a}(X)}{\Delta T} = (1 - e^{-(x+\delta)Pe/2}) \theta(x+\delta) - 1 \quad (7)$$

where we have defined the dimensionless moving frame coordinates:

$$x = \frac{X}{b} \quad y = \frac{Y}{b} \quad (8)$$

and the dimensionless control parameters:

$$\delta = \frac{a}{b} \quad Pe = \frac{2b}{w} = \frac{\ell}{w} = \frac{v\ell}{D} \quad (9)$$

250 where δ is the dimensionless crack lead length and the Péclet number, Pe , is the inverse
 251 dimensionless width of the temperature profile. For later convenience, we have scaled the
 252 parameters with half the column diameter, b , and not the full column diameter, $\ell = 2b$,
 253 as in Eq. (5). The only difference generated is a factor of one half in the exponent of
 254 Eq. (7).

255 In order to determine the crack growth, we are interested in calculating the mode I
 256 stress intensity factor of the crack tips. We therefore need to know how its value depends
 257 on the distance between the crack tips and the temperature front δ . We further need to
 258 know how it depends on the parameters of the temperature front ΔT and Pe as well as
 259 on parameters of the solidifying material itself E , α_T , and $K_{I,c}$. Here E is the Young's
 260 modulus, α_T the coefficient of linear thermal expansion and $K_{I,c}$ the critical mode I stress
 261 intensity factor (fracture toughness).

We assume that the cracks propagate straight, such that the mode II stress intensity factor is always zero. Due to the periodicity in the y -direction, we only need to consider the region $Y \in [-b, b]$ or equivalently $y \in [-1, 1]$, which is colored gray in Figure 3b. It is also assumed, that the changes in the thermal fluxes happen on a time scale much larger than the time needed for the material to reach elastostatic equilibrium. This is a reasonable assumption since the speed of sound in basalt is of the order 10^3 m/s [Gleason, 2010] whereas the speed of the thermal front is of the order 10^{-8} m/s [Hardee, 1980]. We will not consider the effect of temperature dependent elastic parameters. We define the dimensionless stress, σ_{ij} , and strain, ϵ_{ij} :

$$\sigma_{ij} = \frac{\sigma_{IJ}}{E\alpha_T\Delta T} \quad \epsilon_{ij} = \frac{\epsilon_{IJ}}{\alpha_T\Delta T} \quad (10)$$

where i, j runs over the dimensionless parameters x, y and I, J refers to the corresponding parameters X, Y with dimension of length. Under plane stress conditions, the elastostatic mechanical problem is described by three sets of equations:

$$\text{Force balance:} \quad \frac{\partial \sigma_{ij}}{\partial x_j} = 0 \quad (11)$$

$$\epsilon_{xx} = (\sigma_{xx} - \nu \sigma_{yy}) + T_{Pe,\delta}(x)$$

$$\text{Constitutive relations:} \quad \epsilon_{yy} = (\sigma_{yy} - \nu \sigma_{xx}) + T_{Pe,\delta}(x)$$

$$\epsilon_{xy} = (1 + \nu) \sigma_{xy} \quad (12)$$

$$\text{Compatibility:} \quad 2 \frac{\partial^2 \epsilon_{xy}}{\partial x \partial y} = \frac{\partial^2 \epsilon_{xx}}{\partial y^2} + \frac{\partial^2 \epsilon_{yy}}{\partial x^2} \quad (13)$$

In order to calculate the stress tensor components, we make use of the dimensionless Airy stress function, $\phi(x, y)$, which is related to the stress components through the following derivatives:

$$\sigma_{xx} = \frac{\partial^2 \phi}{\partial y^2}, \quad \sigma_{yy} = \frac{\partial^2 \phi}{\partial x^2}, \quad \sigma_{xy} = -\frac{\partial^2 \phi}{\partial x \partial y}. \quad (14)$$

By inserting Eq. (12) in Eq. (13) and simplifying using Eq. (11), we finally obtain from Eq. (14) the equation:

$$\nabla^2 \nabla^2 \phi(x, y) = -\nabla^2 T_{Pe,\delta}(x) \quad (15)$$

The boundary conditions follow from the periodicity of the system and the fact, that σ_{yy} must vanish on the crack faces, whereas the dimensionless displacement in the y -direction,

$u_y = u_Y/b$, must vanish on the rest of the crack line.

$$\sigma_{xy}(x, 1) = \sigma_{xy}(x, -1) = 0 \quad (16)$$

$$\sigma_{xy}(x, 0) = 0 \quad (17)$$

$$u_y(x, 0) = 0 \quad (18)$$

$$\sigma_{yy}(x, 1) = 0 \text{ for } x < 0, \quad u_y(x, 1) = 0 \text{ for } x > 0 \quad (19)$$

4. Results

The calculation of the stress field from Eq. (15) on the entire x -axis is made complicated by the mixed boundary condition in Eq. (19) and has to our knowledge not previously been performed. We have used the Wiener-Hopf method along the lines of [Marder, 1994] to implement the mixed boundary condition, and solve for the stress intensity factor at the crack tip. The solution is derived in Appendix A and we obtain the dimensionless mode I stress intensity factor $\kappa_I = K_I/(E\alpha_T\Delta T\sqrt{b})$:

$$\kappa_I(Pe, \delta) = h_{Pe}(\delta) \quad (20)$$

262 where $\delta = a/b$ is the dimensionless crack lead length and the Péclet number, $Pe = 2b/w$, is
 263 the inverse dimensionless width of the temperature profile. The function $h_{Pe}(\delta)$ is found
 264 analytically in the Appendix, Eq. (A26), and the stress intensity factor is plotted for
 265 different values of Pe and δ in Figure 4.

Crack advance in columnar jointing basalt occurs incrementally, producing striae as mentioned in the introduction. However, we will not try to model this feature, but consider the crack propagation to be in steady state, such that $K_I = K_{I,c}$ always holds at the crack tip, where $K_{I,c}$ is the material dependent critical mode I stress intensity factor (fracture toughness). The crack thus propagates continuously with the same speed as the

temperature front. If we define the dimensionless critical stress intensity factor, $\kappa_{I,c}$, and the mechanical loading length, b_{min} , as:

$$\kappa_{I,c} = \frac{K_{I,c}}{E\alpha_T\Delta T\sqrt{b}} = \sqrt{\frac{b_{min}}{b}} \quad (21)$$

then the fracture criteria $K_I = K_{I,c}$ can be restated as:

$$\kappa_I(Pe, \delta) = \kappa_{I,c} \quad (22)$$

266 and a minimum column spacing, $b = b_{min}$, is obtained in the case of a uniform contraction
 267 where $Pe = 0$ and the stress intensity factor reaches its maximal value $\kappa_I(0, \delta) = 1$ for all
 268 crack lead lengths, δ .

269 For a given material and temperature profile (fixed b_{min} and w), the fracture criterion
 270 in Eq. (22) can be fulfilled for all $b \geq b_{min}$ by changing the crack tip position, $\delta = a/b$,
 271 and thus adjusting $\kappa_I(Pe, \delta)$ in the interval $[0; 1]$. The physical mechanism behind the
 272 continuous set of possible (Pe, δ) -pairs for fixed material and temperature parameters,
 273 can be thought of as follows: If the fracture spacing, and thus the Peclét, Pe , is imagined
 274 to increase slightly, then the resulting fracture density decreases and the stress intensity
 275 at the crack tips increases. To accommodate this change, the crack tips can move further
 276 in to the hot un-contracted region by increasing δ and thus bring the stress intensity at
 277 the crack tips back to the original level.

In summary, the two-dimensional model of an infinite array of cracks predicts, that there is a minimum column diameter for a given material and temperature profile:

$$b \geq b_{min} \quad (23)$$

278 where $b_{min} = (K_{I,c}/E\alpha_T\Delta T)^2$ and the range of b -values fulfilling Eq. (23) are equally
 279 possible within the framework of the model.

280 To test whether a range of column diameters occurs, we have performed a set of dis-
281 crete element simulations (Appendix B). In the simulations the temperature front in
282 Eq. (6) is propagated through a three dimensional linear elastic material. The material
283 is represented by discrete elements, i.e. connected springs which thermally can contract
284 and which can break if a critical stress or strain is reached. An example of the resulting
285 fracture network is shown in Figure 5. The dimensionless fracture toughness, $\kappa_{I,c}$, and
286 the temperature front width, w , are simulation parameters, whereas the column diame-
287 ter, $\langle \ell \rangle$, is measured when the system reaches a state of steady crack propagation with
288 constant column diameter. From the measured column diameter, the Péclet number of
289 the simulation, $Pe = \langle \ell \rangle / w$, can be found.

290 We have performed simulations where the width of the temperature front, w , is either
291 suddenly or slowly increased/decreased for fixed $\kappa_{I,c}$. In general, we observe a corre-
292 sponding increase/decrease in the column diameter such that the Péclet number stays
293 approximately constant. If all column diameters in the range $b \geq b_{min}$ were equally pos-
294 sible, we would expect to see instances where the column width remains constant at the
295 cost of a change in distance between the temperature profile and the crack tips. As w
296 changes, but b stays fixed, the result is a change of the Péclet number. In summary, the
297 simulated systems seem to select one specific column diameter, ℓ , for each temperature
298 profile width, w , leading to a one-to-one correspondence between the Péclet number, Pe ,
299 and the dimensionless fracture toughness, $\kappa_{I,c}$. However, the possibility of a narrow but
300 finite range of allowed Péclet numbers, and thus column widths, can not be ruled out from
301 the present simulations.

302 We expect the approximate one-to-one correspondence between Pe and $\kappa_{I,c}$ to be caused
 303 by a bifurcation instability [*Hofmann et al.*, 2011; *Bahr et al.*, 2009]. If we consider all
 304 pairs of (Pe, δ) fulfilling Eq. (22) there will be a minimum value of the Péclet number
 305 below which the system is unstable to a small advance of one crack tip relative to its
 306 neighbors, leading to a doubling of the column width. It can be motivated, that steady
 307 columnar joint formation with a constant width occurs close to the stability limit, by
 308 considering the cooling history of the system. When cooling is initiated, the cooling
 309 effect of the cracks in the material surface is negligible compared to the external diffusive
 310 cooling from e.g. the underlying ground. As the diffusive cooling front slows down with
 311 time, a series of bifurcation events are induced as the stability limit for the column width
 312 is encountered, and the system coarsens. Eventually, convectional cooling becomes the
 313 dominant cooling mechanism, and the temperature field and crack propagation reaches a
 314 steady state. The column width will thus approximately correspond to the stability limit.

To obtain a quantitative relationship between the column width and the dimensionless
 fracture toughness, we will in the following assume a one-to-one correspondence between
 the Péclet number, Pe , and the fracture toughness, $\kappa_{I,c}$. This assumption together with
 Eq. (22) implies, that δ , must also be a function of the Péclet number. In addition to
 the three-dimensional simulations, we have performed simulations in two dimensions, to
 test more directly the analytical calculations and the relation between Pe and δ . In two
 dimensions, we have measured the average separation between cracks, $\langle \ell \rangle$, and the crack
 lead length, $\langle \delta \rangle$. Figure 6 indicates a power law relation between the Péclet number, Pe ,
 and the crack lead length, δ , measured in two dimensions:

$$\delta = g(Pe) = c_1 Pe^{c_2} \quad (24)$$

315 As the error-bars are large, we propose the coefficients $c_1 = 5.4$ and $c_2 = -1.4$ which are
 316 in agreement with the 2D simulation measurements, see Figure 6, and furthermore yield a
 317 best fit between the pairs of $\kappa_{I,c}$ and measured Pe from the three-dimensional simulations,
 318 see Figure 7. We note that the data in Figure 6 could be consistent with a narrow but
 319 finite range of crack lead lengths, δ , possible for each Péclet number.

Here we assume the power law relation in Eq. (24). The power law relation allows us to replace δ with a function of the Péclet number $\delta = g(Pe)$, and thus analytically obtain a one-to-one relation between the system parameters in $\kappa_{I,c}$, and the Péclet number. The fracture criteria in Eq. (22) can be restated as:

$$f(Pe) = \kappa_I(Pe, g(Pe)) = \kappa_{I,c} \quad (25)$$

320 where we have defined the scaling function $f(Pe) = \kappa_I(Pe, g(Pe))$. The scaling function,
 321 plotted in Figure 7, is in excellent agreement with three-dimensional discrete element
 322 simulations. This supports the validity of a one-to-one relationship between the Péclet
 323 number and the dimensionless fracture toughness, $\kappa_{I,c}$. The scaling function agrees rea-
 324 sonably well with estimates of $\kappa_{I,c}$ and Pe for the Kilauea Iki lava lake and stearic acid,
 325 where the speed, v , of the temperature front has been directly measured. The estimate of
 326 Pe and $\kappa_{I,c}$ for the Kilauea Iki lava lake is based on the parameters listed in Table 1 and
 327 a column diameter assumed similar to that of the Prehistoric Makaopuhi lava lake. The
 328 Kilauea Iki lava lake is to our knowledge the only published field data, where the speed,
 329 v , of the thermal front has been measured directly. The stearic acid estimate of Pe and
 330 $\kappa_{I,c}$ is based on the parameters listed in Table 2.

331 We stress, that the column width ℓ predicted by Eq. (25) is a function of both the
 332 material properties ($E, \alpha_T, D, K_{I,c}$) and the externally imposed cooling conditions ($\Delta T, v$).

4.1. Prediction of the temperature front propagation speed from the scaling function

333 The scaling function, Eq. (25), allows us to estimate the Péclet number of a process
 334 $Pe = f^{-1}(\kappa_{I,c})$, from the dimensionless fracture toughness $\kappa_{I,c} = K_{I,c}/E\alpha_T\Delta T\sqrt{b}$. From
 335 the Péclet number, $Pe = \ell/w = v\ell/D$, the temperature front propagation speed, v , can
 336 be estimated, if the thermal diffusivity, D , and the column diameter, $\ell = 2b$, is known.

337 Figure 8 shows the temperature front speed, v , estimated from our model using the
 338 parameters in Table 3 and field measurements of $\langle\ell\rangle$ for sites in the Columbia River
 339 Basalt Group available from the supplementary material of [Goehring and Morris, 2008].
 340 The corresponding estimated Péclet numbers are in the range $Pe \in [0.2 - 0.3]$.

341 The figure also shows the estimates of v for the same sites based on field measurements
 342 of the striae heights, $\langle s \rangle$, as presented in [Goehring et al., 2009]. The model's estimates,
 343 based on $\langle\ell\rangle$, systematically predict values of v which are a factor two smaller than the
 344 estimates based on $\langle s \rangle$. The two estimates are close, when keeping in mind that the two
 345 methods use independent field data, $\langle\ell\rangle$ and $\langle s \rangle$, and different models for the system. We
 346 propose our model as a way to quickly estimate the temperature front speed, v , when no
 347 striae height measurements are available.

5. Conclusion

348 We have used stearic acid as a new model material for columnar jointing caused by
 349 thermal contraction. If better temperature control is gained in the stearic acid experi-
 350 ments, we expect that our experimental system could further be used to investigate the
 351 entablature formation as well as the possibility of a range of column diameters for each
 352 set of material properties and cooling parameters.

353 Based on numerical simulations and analytical calculations, we argued that one Péclet
 354 number is selected for each dimensionless critical stress intensity factor, though a narrow
 355 finite range of Péclet numbers could not be ruled out.

356 We derived the functional form of the relation between the Péclet number and the
 357 dimensionless critical stress intensity factor and finally showed that our derivations are in
 358 reasonable agreement with data obtained from stearic acid experiments, three-dimensional
 359 numerical simulations and field data. We suggest our scaling function as a quick way to
 360 determine the rate by which the fracture front and therefore the cooling front advances
 361 in a system using as input basic properties of the material, the emplacement temperature
 362 and field measurements of the column diameter. Alternatively, an estimate of the column
 363 diameter can be obtained from the scaling function if the fracture front speed is known.

Appendix A: Analytical solution for the stress intensity factor

A1. The Wiener-Hopf Equation

We want to solve Eq. (15), which is defined on the entire x -axis with the boundary conditions in Eq. (16-19). For convenience, Eq. (15) is here reproduced as Eq. (A1):

$$\nabla^2 \nabla^2 \phi(x, y) = -\nabla^2 T_{Pe, \delta}(x) \quad (\text{A1})$$

and the boundary conditions are reproduced as Eq. (A2-A5):

$$\sigma_{xy}(x, 1) = \sigma_{xy}(x, -1) = 0 \quad (\text{A2})$$

$$\sigma_{xy}(x, 0) = 0 \quad (\text{A3})$$

$$u_y(x, 0) = 0 \quad (\text{A4})$$

$$\sigma_{yy}(x, 1) = 0 \text{ for } x < 0, \quad u_y(x, 1) = 0 \text{ for } x > 0 \quad (\text{A5})$$

364 where x, y are dimensionless coordinates, $\sigma_{ij}, \epsilon_{ij}$ are dimensionless stress and strain,
 365 $T_{Pe,\delta}(x)$ defined in Eq. (7) is the dimensionless temperature front, δ is the dimensionless
 366 distance between the crack tips and the temperature front and Pe is the dimensionless
 367 width of the temperature front.

368 We note, that had we instead of plane stress worked with plain strain conditions, the
 369 modification of the constitutive relations would result in a factor of $1/(1-\nu^2)$ multiplying
 370 the right hand side of Eq. (A1). All calculations to be performed in this section can
 371 therefore easily be modified to a plane strain setting.

If we introduce the partly unknown functions $u_-(x, 1)$ and $\sigma_+(x, 1)$:

$$u_-(x, 1) = \begin{cases} u_y(x, 1) & \text{for } x \leq 0 \\ 0 & \text{for } x > 0 \end{cases} \quad (\text{A6})$$

$$\sigma_+(x, 1) = \begin{cases} 0 & \text{for } x \leq 0 \\ \sigma_{yy}(x, 1) & \text{for } x > 0 \end{cases} \quad (\text{A7})$$

then the boundary condition for $u_y(x, 1)$ in Eq. (A5) can be extended to the entire x -axis
 and restated as:

$$u_y(x, 1) = u_-(x, 1) \text{ for all } x \quad (\text{A8})$$

372 where $u_-(x, 1)$ is partly unknown so far.

Eq. (A1) can be Fourier transformed in the x -direction and turned into a fourth order
 inhomogeneous ODE. We denote the dimensionless transform variable q and the trans-
 formed functions by a tilde:

$$\left(q^4 - 2q^2 \frac{\partial^2}{\partial p^2} + \frac{\partial^4}{\partial p^4} \right) \tilde{\phi}(q, p) = q^2 \tilde{T}_{Pe,\delta}(q) \quad (\text{A9})$$

We now consider the Fourier transform of the functions in Eq. (A6-A7) utilizing that they
 both vanish on half of the x -axis. For the Fourier transform of $\sigma_+(x, 1)$ we use a complex

parameter $q = \alpha + i\tau$, where α and τ are real:

$$\begin{aligned}\tilde{\sigma}_+(q, 1) &= \int_{-\infty}^{\infty} e^{iqx} \sigma_+(x, 1) dx \\ &= \int_0^{\infty} e^{iqx} \sigma_+(x, 1) dx \\ &= \int_0^{\infty} e^{i\alpha x} e^{-\tau x} \sigma_+(x, 1) dx\end{aligned}\tag{A10}$$

373 Assuming that the behavior of $|\sigma_+(x, 1)|$ is $O(e^{\tau_\sigma x})$ as $x \rightarrow \infty$, then the integral in
374 Eq.(A10) converges in the complex half plane given by $\tau > \tau_\sigma$. I.e., $\tilde{\sigma}_+(q, 1)$ is analytic in
375 this half plane.

376 If $\sigma_+(x, 1)$ has algebraic growth, is constant or decays slower than an exponential func-
377 tion for $x \rightarrow \infty$, then $\tau_\sigma = 0$. So the real axis is only a part of the region of analyticity if
378 $\sigma_+(x, 1)$ has exponential decay at infinity.

We can define $\tilde{u}_-(q, 1)$ by doing similar considerations. We know that $u_-(x, 1)$ vanishes
in the uncracked material for $x > 0$:

$$\begin{aligned}\tilde{u}_-(q, 1) &= \int_{-\infty}^{\infty} e^{iqx} u_-(x, 1) dx \\ &= \int_{-\infty}^0 e^{i\alpha x} e^{-\tau x} u_-(x, 1) dx\end{aligned}\tag{A11}$$

379 Assuming the behavior of $|u_-(x, 1)|$ is $O(e^{\tau_u x})$ as $x \rightarrow -\infty$, then the integral in Eq. (A11)
380 converges in the complex half plane given by $\tau < \tau_u$, such that $\tilde{u}_-(q, 1)$ is analytic in this
381 region.

Solving Eq. (A9) with the boundary conditions of Eq. (A2-A4, A8) yields the Wiener-
Hopf Eq. (A12):

$$\tilde{\sigma}_+(q, 1) = D_{Pe,\delta}(q) + F(q)\tilde{u}_-(q, 1)\tag{A12}$$

where $\tilde{u}_-(q, 1)$ is still partly unknown. The functions $F(q)$ and $D_{Pe,\delta}(q)$ are defined as:

$$F(q) = \frac{q}{2} [\coth(q) + q \operatorname{csch}^2(q)] \quad (\text{A13})$$

$$D_{Pe,\delta}(q) = -\tilde{T}_{Pe,\delta}(q) \quad (\text{A14})$$

A2. Solving the Wiener-Hopf Equation

382 The Wiener-Hopf method allows us, to use our knowledge of the asymptotic behavior
 383 of $u_-(x, 1)$ and $\sigma_+(x, 1)$ to express $\tilde{\sigma}_+(q, 1)$ in Eq. (A12) purely in terms of the known
 384 functions $F(q)$ and $D_{Pe,\delta}(q)$ and without reference to the partly unknown $u_-(x, 1)$.

385 The first step is to separate Eq. (A12) into a right hand side analytic in a half plane
 386 $\tau < \tau_u$ and a left hand side analytic in a half plane $\tau > \tau_\sigma$. Provided that the two half
 387 planes overlap, i.e. $\tau_\sigma < \tau_u$, then the right hand side represents the analytic continuation
 388 of the left hand side into the entire complex plane and vice versa.

389 To accomplish the separation of Eq. (A12), we need to factorize the function $F(q)$ into
 390 two parts that are analytic in each their respective half plane of the complex plane. The
 391 function $F(q)$ has poles on the imaginary axis for $q = i\pi n$ with $n \in \mathbb{Z}/\{0\}$ and increases
 392 linearly as $q/2$ for $|q| \rightarrow \infty$.

We choose to factorize $F(q)$ into a fraction $F(q) = F_-(q)/F_+(q)$ where $F_-(q)$ has no poles or zeros for $\tau < \tau_{F_-}$ and $F_+(q)$ has no poles or zeros for $\tau > \tau_{F_+}$, where we again use the complex Fourier variable $q = \alpha + i\tau$. The factorization was performed numerically using 32 Chebyshev polynomials following the strategy of *Liu and Marder* [1991]. The large q behavior of F_+ and F_- was chosen to be:

$$\lim_{|q| \rightarrow \infty} F_+(q) \sim \sqrt{\frac{2}{-iq}} \quad (\text{A15})$$

$$\lim_{|q| \rightarrow \infty} F_-(q) \sim \sqrt{\frac{iq}{2}} \quad (\text{A16})$$

which produces the correct behavior $\lim_{|q| \rightarrow \infty} F(q) \sim q/2$ for large $|q|$. Using the factorized $F(q)$ we can rewrite the Wiener-Hopf Eq. (A12) as:

$$\begin{aligned} \tilde{\sigma}_+(q, 1)F_+(q) &= D_{Pe,\delta}(q)F_+(q) + F_-(q)\tilde{u}_-(q, 1) \\ &= e^{-iq\delta}D_{Pe,0}(q)F_+(q) + F_-(q)\tilde{u}_-(q, 1) \end{aligned} \quad (\text{A17})$$

where we have used the translation properties of the Fourier transform to pull the exponential $e^{-iq\delta}$ out in the last line. We need to separate the product $D_{Pe,0}(q)F_+(q)$ into regions of analyticity. We use the Fourier convolution theorem:

$$\begin{aligned} D_{Pe,0}(q)F_+(q) &= \int_{-\infty}^{\infty} e^{iqx} dx \int_{-\infty}^{\infty} D_{Pe,0}(x')F_+(x-x')dx' \\ &= \int_{-\infty}^{\infty} e^{iqx} h_{Pe}(x) dx \\ &= \int_{-\infty}^0 e^{iqx} h_{Pe}(x) dx + \int_0^{\infty} e^{iqx} h_{Pe}(x) dx \\ &= h_-(q) + h_+(q) \end{aligned} \quad (\text{A18})$$

Where $h_+(q)$ does not have any poles in the upper $\tau > \tau_{h+}$ half of the complex plane and $h_-(q)$ does not have any poles in the lower $\tau < \tau_{h-}$ half of the complex plane. With this factorization, the Wiener-Hopf Eq. (A17) takes the form:

$$\tilde{\sigma}_+(q, 1)F_+(q) - h_+(q)e^{-iq\delta} = h_-(q)e^{-iq\delta} + F_-(q)\tilde{u}_-(q, 1) \quad (\text{A19})$$

The left hand side is analytic in the upper half plane $\tau > \max(\tau_\sigma, \tau_{F+}, \tau_{f+})$, and the right hand side is analytic in a lower half plane $\tau < \min(\tau_u, \tau_{F-}, \tau_{f-})$. Provided that the right hand side and the left hand side overlap in some non-empty open subset like a line or a small area, they are each others analytical continuation into the other half plane and

equal to the same entire function $W(q)$:

$$\begin{aligned}\tilde{\sigma}_+(q, 1)F_+(q) - h_+(q)e^{-iq\delta} &= h_-(q)e^{-iq\delta} + F_-(q)\tilde{u}_-(q, 1) \\ &= W(q)\end{aligned}\tag{A20}$$

393 We expect that $u_y(x, b)$ goes to a constant for $x \rightarrow \infty$ which means that $\tau_u = 0$. There
 394 will be an overlap of the two regions of analyticity if $\sigma_{yy}(x, 1)$ has just a slight exponential
 395 decay for $x \rightarrow \infty$, such that $\tau_\sigma = -\epsilon$ where ϵ is a small positive real number. The overlap
 396 is depicted as the gray shaded area in Figure 9 and an overview of the regions of analyticity
 397 is shown in Table 4. It is not physically unreasonable to expect a slight exponential decay
 398 of $\sigma_{yy}(x, 1)$ as $x \rightarrow \infty$, since we know $\sigma_{yy}(x, 1)$ does decay in this limit.

Assuming $\tau_\sigma = -\epsilon$, the function $W(q)$ is entire. To determine the constant value of $W(q)$ we use Abel theorems, which relate the asymptotic behaviors of a function $g(r)$ and its one sided Fourier transforms $\tilde{g}_+(q)$ or $\tilde{g}_-(q)$. We will use the following Abel theorem [Freund, 1990, Sec. 1.3] rewritten for a plus type Fourier transform with $q = \alpha + i\tau$, where both α and τ are real:

$$\lim_{x \rightarrow 0^+} \Gamma(1 + \gamma)x^{-\gamma}g(x) = \lim_{\tau \rightarrow +\infty} (-iq)^{1+\gamma}g_+(q)\tag{A21}$$

Which is valid for $\gamma > -1$. We can extract the asymptotic behavior of the Fourier transformed stress function using the Abel theorem:

$$\lim_{x \rightarrow 0^+} \sigma_{yy}(x, 1) \sim \lim_{x \rightarrow 0^+} \frac{1}{\sqrt{x}} \Rightarrow \lim_{\tau \rightarrow +\infty} \sigma_+(q, 1) \sim \lim_{\tau \rightarrow +\infty} \frac{1}{\sqrt{-iq}}\tag{A22}$$

From the behavior of $F_+(q)$ and $D_{Pe,0}(q)$ we directly have:

$$\lim_{|q| \rightarrow \infty} h_+(q) \sim \lim_{|q| \rightarrow \infty} \sqrt{\frac{2}{-iq}} \left(\frac{1}{iq} \right)\tag{A23}$$

If we consider the left hand side of Eq. (A20), using the asymptotic results of Eq. (A15, A22, A23) we get:

$$\begin{aligned}
\lim_{\tau \rightarrow +\infty} W(q) &= \lim_{\tau \rightarrow +\infty} (\tilde{\sigma}_+(q, 1)F_+(q) - h_+(q)) \\
&\sim \lim_{\tau \rightarrow +\infty} \left[\frac{1}{\sqrt{-iq}} \cdot \sqrt{-\frac{2}{iq}} - \sqrt{\frac{2}{-iq}} \left(\frac{1}{iq} \right) \right] \\
&= \lim_{\tau \rightarrow +\infty} \left[\frac{\sqrt{2}}{\tau - i\alpha} + \sqrt{\frac{2}{\tau - i\alpha}} \left(\frac{1}{\tau - i\alpha} \right) \right] \\
&= 0
\end{aligned} \tag{A24}$$

Now, $W(q)$ is analytic in the entire plane, bounded and equal to zero at infinity. Therefore, by Liouville's Theorem, it must be identical zero in the entire plane. This allows us to finally determine $\tilde{\sigma}_+(q, 1)$ from Eq. (A20) without any reference to the partly unknown $\tilde{u}_-(q, 1)$:

$$\begin{aligned}
\tilde{\sigma}_+(q, 1) &= \frac{1}{F_+(q)} h_+(q) e^{-iq\delta} \\
&= \frac{1}{F_+(q)} \int_0^\infty dx e^{iqx} h_{Pe}(x + \delta) \\
&= \frac{1}{F_+(q)} \int_{-\infty}^\infty dx e^{iqx} \theta(x) h_{Pe}(x + \delta)
\end{aligned} \tag{A25}$$

We note, that from Eq. (A18) we can also express $h_{Pe}(x)$ as:

$$h_{Pe}(x) = \int_{-\infty}^\infty \frac{dq}{2\pi} e^{-iqx} F_+(q) D_{Pe,0}(q) \tag{A26}$$

399 where the inverse Fourier transform integral has to be performed within the strip of
400 analyticity of the integrand.

A3. Extracting the stress intensity factor

401 The Abel theorems in Eq. (A21) allow us to infer the $x \rightarrow 0^+$ behavior of $\sigma_{yy}(x, 1)$ from
402 the $\tau \rightarrow \infty$ behavior of $\tilde{\sigma}_+(q, 1)$, where again $q = \alpha + i\tau$.

We define the dimensionless mode I stress intensity factor κ_I as:

$$\kappa_I(\delta) = \lim_{x \rightarrow 0^+} \sqrt{2\pi} x^{1/2} \sigma_{yy}(x, 1) \quad (\text{A27})$$

$$= \lim_{\tau \rightarrow +\infty} \frac{\sqrt{2\pi}}{\Gamma\left(\frac{1}{2}\right)} (-iq)^{1/2} \tilde{\sigma}_+(q, 1) \quad (\text{A28})$$

$$= \lim_{\tau \rightarrow +\infty} \sqrt{-2iq} \tilde{\sigma}_+(q, 1) \quad (\text{A29})$$

To go from Eq. (A27) to Eq. (A28), we have used the Abel theorem in Eq. (A21) for $\gamma = -1/2$. From Eq. (A25), we see that the large q behavior of $\tilde{\sigma}_+(q, 1)$ is partly due to the $1/F_+(q)$ factor and partly due to the integrand. The large q behavior of the integrand in Eq. (A25) is governed by the step function discontinuity of the integrand at $x = 0$.

The large q behavior of the integrand becomes:

$$\lim_{|q| \rightarrow \infty} \int_{-\infty}^{\infty} dx e^{iqx} \theta(x) h_{Pe}(x + \delta) = \lim_{|q| \rightarrow \infty} \left(\frac{-1}{iq} \right) h_{Pe}(\delta) \quad (\text{A30})$$

where the Fourier transform of the step function $\theta(x)$ is $-1/iq$ and exists for $\tau > 0$. The large q behavior of $F_+(q)$ we already know from Eq. (A15). Collecting our knowledge on $\tilde{\sigma}_+(q, 1)$ we arrive at:

$$\begin{aligned} \kappa_I(\delta) &= \lim_{\tau \rightarrow +\infty} \sqrt{-2iq} \sqrt{\frac{-iq}{2}} \left(\frac{-1}{iq} \right) h_{Pe}(\delta) \\ &= \lim_{\tau \rightarrow +\infty} \sqrt{2(\tau - i\alpha)} \sqrt{\frac{\tau - i\alpha}{2}} \left(\frac{1}{\tau - i\alpha} \right) h_{Pe}(\delta) \\ &= h_{Pe}(\delta) \end{aligned} \quad (\text{A31})$$

403 This is the result stated in Eq. (20) of the main text.

Appendix B: Three-dimensional discrete element simulations of the columnar joint formation

To model the cracking of an elastic medium, we use a discrete element method with nodes arranged in a cubic lattice with a lattice constant L^0 . The nodes are interacting

with their nearest-neighbors (NN) and next-nearest-neighbors (NNN) through Hookean springs with spring constants k_1 and k_2 for NNs and NNNs, respectively. The spring connecting the nodes i and j has an equilibrium length L_{ij}^{eq} and holds an elastic energy quadratic in the deviation from the equilibrium length,

$$U_{ij} = \frac{1}{2}k_{ij}(L_{ij} - L_{ij}^{eq})^2 \quad (\text{B1})$$

where \mathbf{x}_i denotes the position of the i 'th node and $L_{ij} = |\mathbf{x}_i - \mathbf{x}_j|$. The total energy of the system is given by the sum over all springs $U^{tot} = \sum U_{ij}$. The elasticity tensor corresponding to these interactions can be written in the form [Hayakawa, 1994]:

$$C_{iiii} = (k_1 + 2k_2)/L^0 \quad (\text{B2})$$

$$C_{iijj} = C_{ijji} = C_{ijij} = k_2/L^0. \quad (\text{B3})$$

The thermal contraction of the system is modeled by changing the local equilibrium distance between the nodes. Like in the previous section, we shall consider a contraction front on the form of Eq. (6):

$$L_{ij}^{eq}(X, X_0) = L_{ij}^0 \left[1 + \alpha_T \Delta T \left(1 - e^{-\frac{X-X_0}{w}} \right) \theta(X - X_0) - \alpha_T \Delta T \right] \quad (\text{B4})$$

where $X_0 = vt = \frac{D}{w}t$ is the position of the temperature front, which moves through the system with time. Since elastic relaxation happens many orders of magnitude faster than thermal relaxation, the simulations proceed by advancing the contraction front a length dX_0 , relaxing the system to elastostatic equilibrium, and repeating the process. The value of dX_0 does not affect the resulting fracture pattern. The state of elastostatic equilibrium or force balance is reached by minimizing the elastic energy, i.e. finding the lattice configuration for which $\nabla U = \nabla \sum U_{ij} = 0$. To that end, we apply a conjugate

gradient method in the multidimensional configuration space. In the simulations, we use a failure criterion where an elastic bond in the lattice is broken when it is strained, ϵ_{ij} , beyond a critical strain ϵ_c :

$$\epsilon_{ij} > \epsilon_c. \tag{B5}$$

404 With this threshold, bonds do not break during compression, i.e. the fractures forming
 405 the columnar joints will mostly grow at the trailing edge of the contraction front. Note,
 406 that while this asymmetry in the fracture criterion have little impact on the morphology
 407 of the steady state patterns, it may influence the fracture patterns formed close to the
 408 boundary of the system, i.e. where the front is initiated.

409 If more than one bond is strained beyond the critical level, the bond with the highest
 410 strain is broken and the lattice is relaxed to the new state of elastostatic equilibrium. We
 411 then check whether other bonds still exceed the critical stress. If a bond still exceeds
 412 the critical stress the process is repeated until no such bond exists and then finally we
 413 advance the contraction front by a small increment, dX_0 . In that way, bonds are broken
 414 one-by-one until none of them exceeds the critical strain.

415 Note that in the simulations the temperature profile starts out with the steady state
 416 shape and therefore the initial cracks nucleating at the surface of the simulation system
 417 might not have any resemblance to the columns close to the cooling surface in real system.
 418 After a transient dynamics over a length of approximately $2w$, the cracks in the simulations
 419 form a regular polygonal pattern equivalent to the columnar joints. An example of a
 420 simulation is shown in Figure 5. When the regular polygonal crack pattern has formed,
 421 then the average column diameter $\langle \ell \rangle$ is measured. From this measurement, the Péclet
 422 number $Pe = \langle \ell \rangle / w$ for the simulation can be determined.

423 The fracture criterion $K_I = K_{I,c}$ of section 4 is in the simulations implemented through
 424 a critical strain. The dimensionless critical stress intensity factor is related to the critical
 425 strain as: $\kappa_{I,c} = K_{I,c}/(E\alpha_T\Delta T\sqrt{b}) = \epsilon_c/(\alpha_T\Delta T)$. This should not affect the above
 426 observations.

Appendix C: Three-dimensional finite element simulations of the columnar joint formation

427 To model the cracking of an elastic medium and test the results of the discrete element
 428 method in Appendix B we use the finite element method (FEM). The material undergoing
 429 cooling is approximated by a box $[0, 4] \times [0, 1] \times [0, 1]$ with periodic boundary conditions
 430 applied on the faces parallel to the X -axis. The computational domain is finely discretized
 431 using tetrahedral elements (4 million tetrahedra). We assume the material to be isotropic
 432 and Cauchy elastic in the simulation, with the Young's modulus E and Poisson ratio
 433 $\nu = 0.25$. The assumption of small displacements is valid in the context of columnar joint
 434 formation and the elasticity model is appropriate for simulating infinite systems.

435 We use the von Mises yield criterion, which states that failure occurs when the von Mises
 436 stress, σ_M , exceeds the material's yield strength, σ_c , chosen in simulation to be equal
 437 $\sigma_c = 0.01E$. We use a standard, linear Galerkin method to discretize the constitutive
 438 equation.

The propagating temperature front and corresponding thermal contraction are modeled as a body force:

$$\beta(X, X_0) = \alpha_T\Delta T \left(1 - \exp^{-(X-X_0)/w}\right) \theta(X - X_0) - \alpha_T\Delta T \quad (C1)$$

439 where the maximum contraction is $\alpha_T\Delta T = 0.2$, the contraction front is located at $X_0 =$
 440 $vt = \frac{D}{w}t$ and the slope $1/w$ varies between 12 and 18. The simulation method at each

441 time step advances the contraction front a step dX_0 , updates the equilibrium von Mises
 442 stress values, and proceeds to fracture resolution. The fracture resolution is performed
 443 by finding the element with the maximum von Mises stress exceeding σ_c and removing
 444 it from the computational mesh (by labeling it as air). This is followed by reassembling
 445 the stiffness matrix and re-equilibrating the system. Those two steps are then repeated
 446 as long as there are elements with $\sigma^M > \sigma_c$ in the mesh. Re-equilibration, which amounts
 447 to solving the constitutive equations with a new stiffness matrix, is a computationally
 448 intensive process hence, in order to improve the method's performance we introduce two
 449 simplifications:

- 450 • System relaxation in the fracture resolution step is performed on a submesh composed
 451 of elements lying in the X -distance 0.1 from the temperature front (which is equivalent
 452 to treating the excluded region as fluid).

- 453 • Instead of only removing a single element at a time, all elements whose von Mises
 454 stress are greater than $\gamma\sigma_c$, $\gamma > 1$ are all removed at once, where γ is chosen in a way
 455 that it does not affect the resulting fracture pattern (determined in our simulation to be
 456 $\gamma = 1.1$).

457 The resulting set of removed tetrahedra displayed in Figure 10 gives a representa-
 458 tion of the columnar fracturing pattern, and can be used to measure the typical col-
 459 umn diameter $\langle \ell \rangle$. The FEM results for pairs of $(Pe, \kappa_{I,c})$ obtained for fixed w and
 460 $\kappa_{I,c} = K_{I,c}/(E\alpha_T\Delta T\sqrt{b}) = \sigma_c/(E\alpha_T\Delta T)$ are in agreement with the discrete element sim-
 461 ulation results, see Figure 7. In the figure, $\kappa_{I,c}$ is multiplied with $(1 - \nu)$ to be comparable
 462 with the scaling function which is derived for 2D.

463 **Acknowledgments.** This study was supported by the grant Earth Patterns by Villum
464 Fonden. Fabrice Mortessagne is thanked for his support of the project and the CNRS is
465 thanked for financial support. The data for this paper are available by contacting the
466 corresponding author at mathies@nbi.dk.

References

- 467 Bahr, H.-A., M. Hofmann, H.-J. Weiss, U. Bahr, G. Fischer, and H. Balke (2009), Diam-
468 eter of basalt columns derived from fracture mechanics bifurcation analysis, *Physical*
469 *Review E*, *79*(5), 056,103, doi:10.1103/PhysRevE.79.056103.
- 470 Bohn, S., S. Douady, and Y. Couder (2005), Four Sided Domains in Hierar-
471 chical Space Dividing Patterns, *Physical Review Letters*, *94*(5), 054,503, doi:
472 10.1103/PhysRevLett.94.054503.
- 473 Bosshard, S. A., H. B. Mattsson, and G. Hetényi (2012), Origin of internal flow structures
474 in columnar-jointed basalt from Hrepphólar, Iceland: I. Textural and geochemical char-
475 acterization, *Bulletin of Volcanology*, *74*(7), 1645–1666, doi:10.1007/s00445-012-0623-z.
- 476 Budkewitsch, P. (1994), Modelling the evolution of columnar joints, *Journal of Volcanology*
477 *and Geothermal Research*, *59*(3), 219–239, doi:10.1016/0377-0273(94)90092-2.
- 478 Cohen, Y., J. Mathiesen, and I. Procaccia (2009), Drying patterns: Sensitivity to residual
479 stresses, *Physical Review E*, *79*(4), 046,109.
- 480 Degraff, J. M., and A. Aydin (1993), Effect of thermal regime on growth increment and
481 spacing of contraction joints in basaltic lava, *Journal of Geophysical Research: Solid*
482 *Earth*, *98*(B4), 6411–6430, doi:10.1029/92JB01709.

- 483 Freund, L. B. (1990), *Dynamic Fracture Mechanics*, Cambridge University Press, Cam-
484 bridge.
- 485 Gilman, J. J. (2009), Basalt columns: Large scale constitutional supercool-
486 ing?, *Journal of Volcanology and Geothermal Research*, 184(3–4), 347–350, doi:
487 10.1016/j.jvolgeores.2009.04.017.
- 488 Gleason, A. E. (2010), Elasticity of Materials at High Pressure, Ph.D. thesis, University
489 of California, Berkeley.
- 490 Goehring, L., and S. W. Morris (2008), Scaling of columnar joints in basalt, *Journal of*
491 *Geophysical Research: Solid Earth*, 113(B10), B10,203, doi:10.1029/2007JB005018.
- 492 Goehring, L., S. W. Morris, and Z. Lin (2006), Experimental investigation of the scaling of
493 columnar joints, *Physical Review E*, 74(3), 036,115, doi:10.1103/PhysRevE.74.036115.
- 494 Goehring, L., L. Mahadevan, and S. W. Morris (2009), Nonequilibrium scale selection
495 mechanism for columnar jointing, *Proceedings of the National Academy of Sciences*,
496 106(2), 387–392, doi:10.1073/pnas.0805132106.
- 497 Goehring, L., A. Nakahara, T. Dutta, S. Kitsunozaki, and S. Tarafdar (2015), *Desiccation*
498 *Cracks and their Patterns: Formation and Modelling in Science and Nature*, John Wiley
499 & Sons.
- 500 Groisman, A., and E. Kaplan (1994), An Experimental Study of Cracking Induced by
501 Desiccation, *EPL (Europhysics Letters)*, 25(6), 415, doi:10.1209/0295-5075/25/6/004.
- 502 Grossenbacher, K. A., and S. M. McDuffie (1995), Conductive cooling of lava: colum-
503 nar joint diameter and stria width as functions of cooling rate and thermal gradient,
504 *Journal of Volcanology and Geothermal Research*, 69(1–2), 95–103, doi:10.1016/0377-
505 0273(95)00032-1.

- 506 Guy, B. (2010), Comments on “Basalt columns: Large scale constitutional supercool-
507 ing? by John Gilman (JVGR, 2009) and presentation of some new data [J. Volcanol.
508 Geotherm. Res. 184 (2009), 347–350], *Journal of Volcanology and Geothermal Research*,
509 194(1–3), 69–73, doi:10.1016/j.jvolgeores.2009.09.021.
- 510 Hardee, H. C. (1980), Solidification in Kilauea Iki lava lake, *Journal of Volcanology and*
511 *Geothermal Research*, 7(3–4), 211–223, doi:10.1016/0377-0273(80)90030-X.
- 512 Hayakawa, Y. (1994), Pattern selection of multicrack propagation in quenched crystals,
513 *Physical Review E*, 50(3), R1748–R1751, doi:10.1103/PhysRevE.50.R1748.
- 514 Hetényi, G., B. Taisne, F. Garel, É. Médard, S. Bosshard, and H. B. Mattsson (2012),
515 Scales of columnar jointing in igneous rocks: field measurements and controlling factors,
516 *Bulletin of Volcanology*, 74(2), 457–482, doi:10.1007/s00445-011-0534-4.
- 517 Hofmann, M., H.-A. Bahr, H.-J. Weiss, U. Bahr, and H. Balke (2011), Spacing of crack
518 patterns driven by steady-state cooling or drying and influenced by a solidification
519 boundary, *Physical Review E*, 83(3), 036,104, doi:10.1103/PhysRevE.83.036104.
- 520 Hofmann, M., R. Anderssohn, H.-A. Bahr, H.-J. Weiß, and J. Nellesen (2015),
521 Why Hexagonal Basalt Columns?, *Physical Review Letters*, 115(15), 154,301, doi:
522 10.1103/PhysRevLett.115.154301.
- 523 Iyer, K., B. Jamtveit, J. Mathiesen, A. Malthe-Sørensen, and J. Feder (2008), Reaction-
524 assisted hierarchical fracturing during serpentinization, *Earth and Planetary Science*
525 *Letters*, 267(3), 503–516.
- 526 Jagla, E. A., and A. G. Rojo (2002), Sequential fragmentation: The origin
527 of columnar quasihexagonal patterns, *Physical Review E*, 65(2), 026,203, doi:
528 10.1103/PhysRevE.65.026203.

- 529 Kantha, L. H. (1981), ‘Basalt fingers’ – origin of columnar joints?, *Geological Magazine*,
530 118(03), 251–264, doi:10.1017/S0016756800035731.
- 531 Liu, X., and M. Marder (1991), The energy of a steady-state crack in a strip, *Journal of the*
532 *Mechanics and Physics of Solids*, 39(7), 947–961, doi:10.1016/0022-5096(91)90013-E.
- 533 Mallet, R. (1875), On the origin and mechanism of production of the prismatic (or
534 columnar) structure of basalt, *Philosophical Magazine Series 4*, 50(329), 122–135, doi:
535 10.1080/14786447508641268.
- 536 Marder, M. (1994), Instability of a crack in a heated strip, *Physical Review E*, 49(1),
537 R51–R54, doi:10.1103/PhysRevE.49.R51.
- 538 Müller, G. (1998), Experimental simulation of basalt columns, *Journal of Volcanology and*
539 *Geothermal Research*, 86(1–4), 93–96, doi:10.1016/S0377-0273(98)00045-6.
- 540 Müller, G. (2001), Experimental simulation of joint morphology, *Journal of Structural*
541 *Geology*, 23(1), 45–49, doi:10.1016/S0191-8141(00)00104-8.
- 542 Peck, D. L., and T. Minakami (1968), The Formation of Columnar Joints in the Upper
543 Part of Kilauean Lava Lakes, Hawaii, *Geological Society of America Bulletin*, 79(9),
544 1151–1166, doi:10.1130/0016-7606(1968)79[1151:TFOCJI]2.0.CO;2.
- 545 Phillips, J. C., M. C. S. Humphreys, K. A. Daniels, R. J. Brown, and F. Witham (2013),
546 The formation of columnar joints produced by cooling in basalt at Staffa, Scotland,
547 *Bulletin of Volcanology*, 75(6), 1–17, doi:10.1007/s00445-013-0715-4.
- 548 Røyne, A., B. Jamtveit, J. Mathiesen, and A. Malthe-Sørenssen (2008), Controls on rock
549 weathering rates by reaction-induced hierarchical fracturing, *Earth and Planetary Sci-*
550 *ence Letters*, 275(3), 364–369.

- 551 Ryan, M. P., and C. G. Sammis (1978), Cyclic fracture mechanisms in cooling
552 basalt, *Geological Society of America Bulletin*, 89(9), 1295–1308, doi:10.1130/0016-
553 7606(1978)89<1295:CFMICB>2.0.CO;2.
- 554 Ryan, M. P., and C. G. Sammis (1981), The glass transition in basalt, *Journal of Geo-*
555 *physical Research: Solid Earth*, 86(B10), 9519–9535, doi:10.1029/JB086iB10p09519.
- 556 Spry, A. (1962), The origin of columnar jointing, particularly in basalt flows, *Journal of*
557 *the Geological Society of Australia*, 8(2), 191–216, doi:10.1080/14400956208527873.
- 558 Tomkeieff, S. I. (1940), The basalt lavas of the Giant’s Causeway district of Northern
559 Ireland, *Bulletin Volcanologique*, 6(1), 89–143, doi:10.1007/BF02994875.
- 560 Toramaru, A., and T. Matsumoto (2004), Columnar joint morphology and cooling rate:
561 A starch-water mixture experiment, *Journal of Geophysical Research: Solid Earth*,
562 109(B2), B02,205, doi:10.1029/2003JB002686.

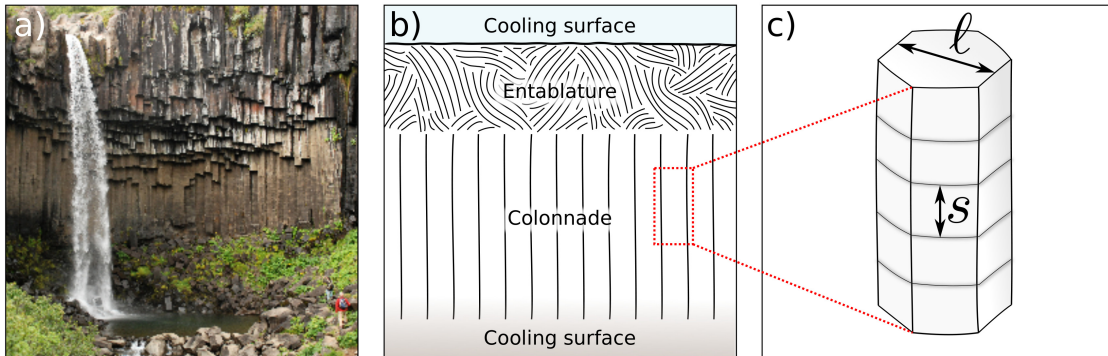


Figure 1. *a)* Exposed columnar joint formation at Svartifoss, Iceland. *b)* Sketch of a columnar jointed basalt flow cooled from the top and the bottom. The colonnade contains regular polygonal columns with a more or less constant diameter, whereas the entablature region is highly disorganized with small and curvy columns. *c)* The diameter, ℓ , of the column is approximately constant over most of its height. The incremental crack propagation leaves striations on the faces of the column, here indicated by gray lines. The distances between striations marks, s , is the vertical distance the crack front propagated in one crack advance event.

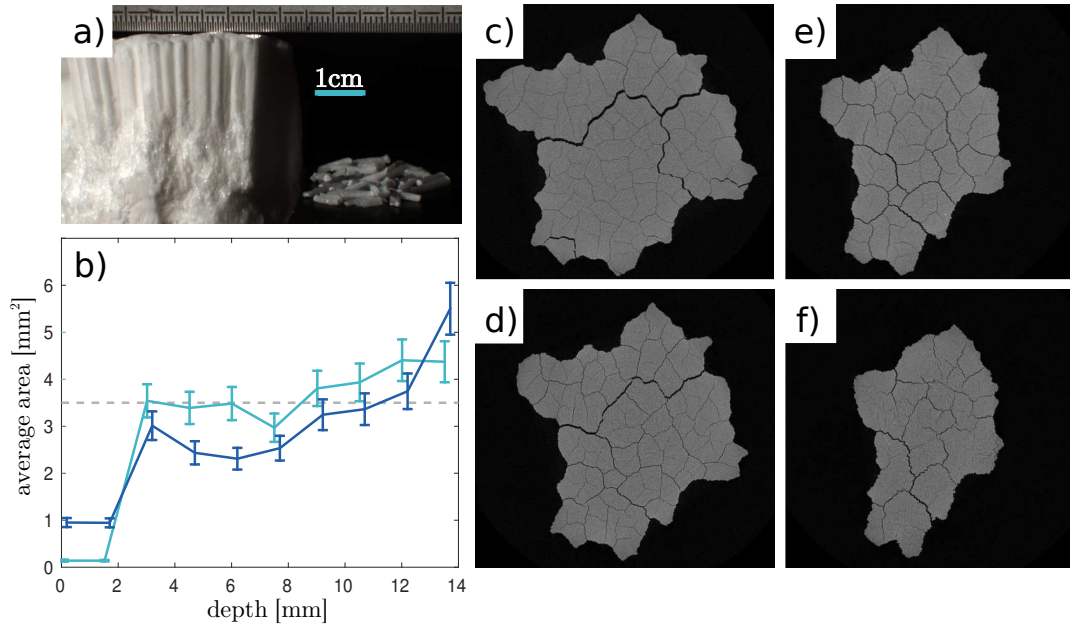


Figure 2. *a)* Columnar joints in solid stearic acid. The structure is obtained by breaking a post-solidified sample, individual columns can easily be detached. The structure initiates at the contact with the aluminum can (here top) and propagates to a depth of about 2 cm. No organized structure is observed beyond (here bottom). *b)* X-ray microtomography analysis. The average area of the columns as a function of the depth is plotted for two samples with identical parameters inside a cylindrical aluminum can. About 3 mm from the cooling surface, the area stabilizes and is approximately constant as indicated by the gray line. *c-f)* X-ray microtomography scans of a stearic acid sample in a cylindrical aluminum can. Depths from the cooling surface are: *c)* 3.6 mm, *d)* 7.2 mm, *e)* 10.8 mm and *f)* 14.4 mm.

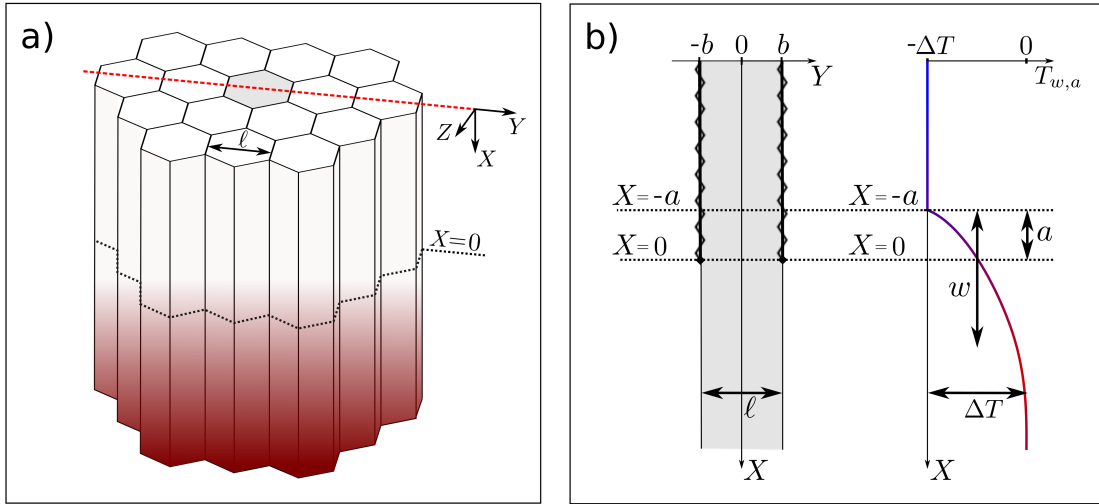


Figure 3. *a)* Infinite array of perfectly hexagonal columns with diameter $\ell = 2b$. The columns extend from $X = -\infty$ to $X = 0$ and the uncracked material extends from $X = 0$ to $X = \infty$. The front of crack tips is indicated with a black dashed line and is located at $X = 0$. The system is subject to a temperature field $T_{w,a}(X)$, which varies only in the X -direction. Red indicates hot regions and white indicates colder regions. We emphasize that the coordinate system (X, Y, Z) is moving at speed v with the convection zone. It is only in this moving frame, that the temperature front has a constant shape. *b)* The gray strip results from a vertical cut along the red dashed line in Figure 3a. We only need to consider one column, since the 2D plane cut is periodic in the y -direction. The gray strip is infinite in the X -direction and periodic in the Y -direction with $Y = +b$ equal to $Y = -b$. The semi-infinite cracks centered at $Y = \pm b$ are indicated with zigzag lines and extend from $X = -\infty$ to $X = 0$. The crack tips at $X = 0$ are indicated with diamonds. The strip is subject to the temperature profile $T_{w,a}(X)$ in Eq. (6), where a is the signed distance between the crack tips and the temperature front, w is the width of the temperature profile and $\Delta T = T_1 - T_0$ is the maximal temperature difference with respect to the temperature of the undeformed state. Note, that a in principle can be both positive and negative in the model, but positive a is the case relevant for columnar

jointing in igneous rock and was assumed when producing this drawing.

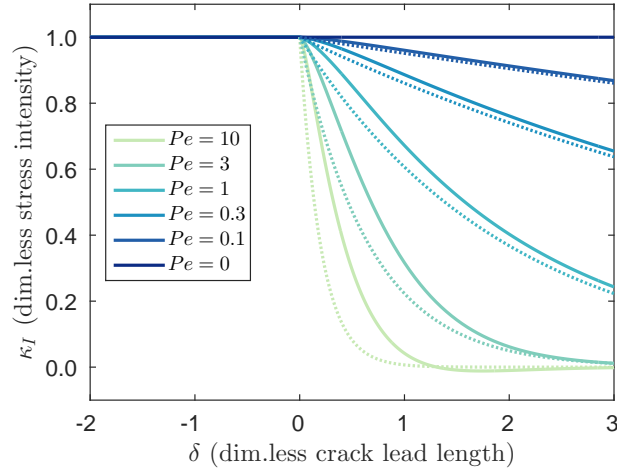


Figure 4. The dimensionless mode-I stress intensity factor, κ_I , as a function of the distance between the temperature front and the crack tips, $\delta = a/b$, for different Péclet numbers, $Pe = 2b/w$. The analytical solution is represented by solid lines and the dotted lines indicate minus the dimensionless temperature front, $-T_{Pe,\delta}(x=0)$. For small Péclet numbers, the temperature gradient is small and a crack tip located at $x=0$, a distance δ ahead of the temperature profile, experiences an essentially uniform contraction equal to $-T_{Pe,\delta}(x=0)$. For larger Péclet numbers, the temperature gradient kicks in and the stress intensity factor ceases to be equal to $-T_{Pe,\delta}(x=0)$. The value $\kappa_I = 1$ corresponds to the stress intensity factor for a uniform temperature field ($Pe = 0$).

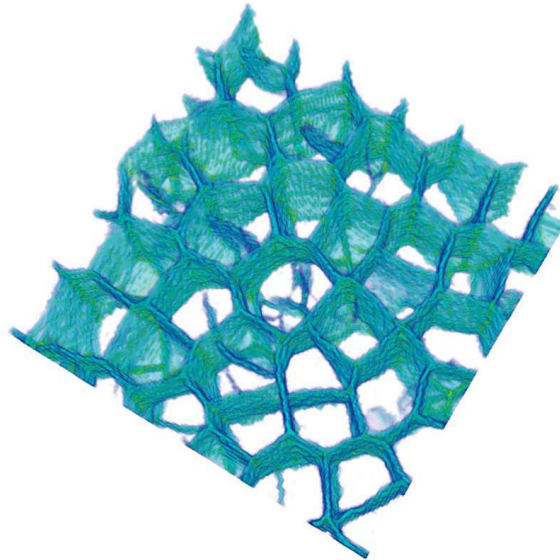


Figure 5. Example of a discrete element simulation of columnar jointing. The system size is $140 \times 140 \times 100$ and the parameters used are $w = 5$, $\alpha_T \Delta T = 0.02$ and $\epsilon_c = 0.009$. The simulations are described in Appendix B. Similar simulations were carried out in 2D to produce Figure 6.

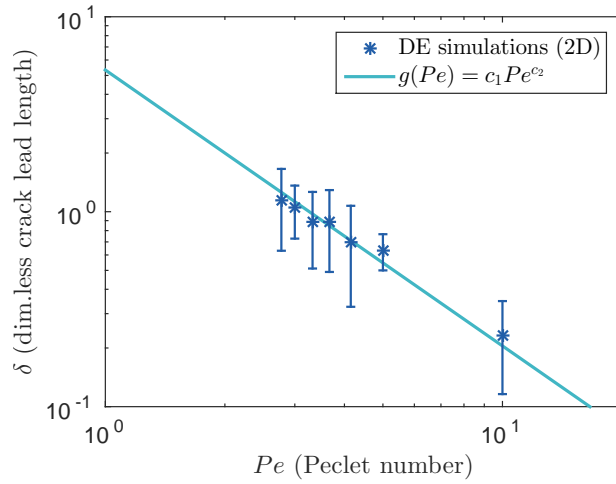


Figure 6. Discrete element simulations were performed in 2D and the average column diameter, $\langle \ell \rangle$, as well as the average crack lead length, $\langle a \rangle$, were measured. We observe a power law relation between the Péclet number, $Pe = \langle \ell \rangle / w$, and the crack lead length, $\delta = \langle a \rangle / (\langle \ell \rangle / 2)$. The plotted power law is given by $\delta = g(Pe) = c_1 Pe^{c_2}$ with $c_1 = 5.4$ and $c_2 = -1.4$.

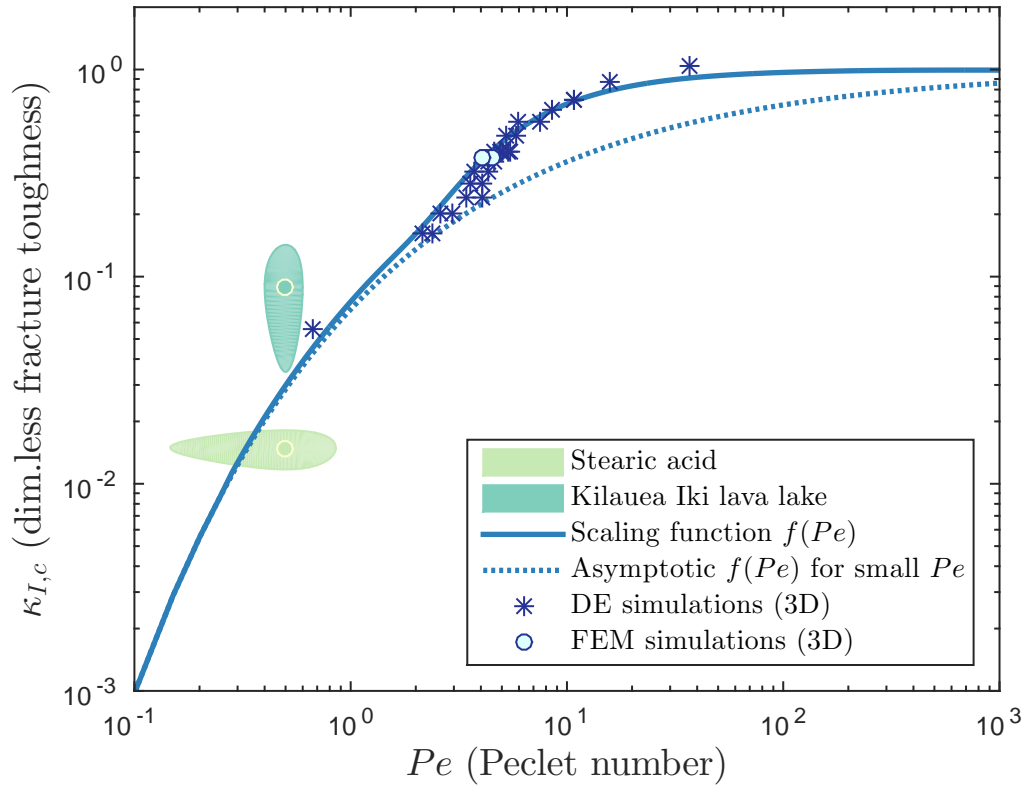


Figure 7. The three-dimensional discrete element (DE) simulations are in good agreement with the scaling function $f(Pe)$. In the simulations, $\kappa_{I,c}$ and the temperature front width, w , are simulation parameters, whereas the column width, $\langle \ell \rangle$, and thus the Péclet number, $Pe = \langle \ell \rangle / w$, is measured. A few finite element (FEM) simulations of the crack propagation (Appendix C) were run to check the validity of the discrete element scheme. The results are displayed as full circles and correspond closely to the DE simulations. For small Péclet numbers, the stress intensity factor approaches $-T_{Pe,\delta}(x=0)$ as seen in Figure 4, and the asymptotic behavior of the scaling function becomes $f(Pe) \rightarrow -T_{Pe,g(Pe)}(x=0)$ for small Péclet numbers. The scaling function is also in reasonable agreement with data from the stearic acid experiments and estimates for the Kilauea Iki lava lake, where the velocity of the temperature front was measured directly.

Table 1. Physical properties of basalt and parameters of the temperature front at the Kilauea Iki lava lake^a

Property	Symbol	Value	Source
Fracture toughness	$K_{I,c}$	$2.2 \text{ MPa}\sqrt{\text{m}}$	1
Young's modulus	E	$(54.5 \pm 5.5) \text{ GPa}$	2 ^b
Poisson's ratio	ν	0.22	2
Linear coefficient of thermal expansion	α_T	$(5 \pm 3) \cdot 10^{-6}/^\circ\text{C}$	2
Thermal diffusivity	D	$5 \cdot 10^{-7} \text{ m}^2/\text{s}$	3
Max. temperature difference	ΔT	970°C	3
Temperature front speed	v	$6.7 \cdot 10^{-8} \text{ m/s}$	3
Column diameter	ℓ	$(3.5 \pm 0.4) \text{ m}$	2 ^c

^a The values are taken from 1: *Degraff and Aydin* [1993], 2: *Ryan and Sammis* [1981] and 3: *Hardee* [1980].

^b A 10% deviation of E is inferred from Figure 2 of *Ryan and Sammis* [1981].

^c ℓ is the column diameter of the Prehistoric Makaopuhi lava lake, which is assumed similar to the Kilauea Iki lava lake. The average column face width has been converted to diameter using a hexagonal column shape.

Table 2. Physical properties of stearic acid and parameters of the temperature front^a

Property	Symbol	Value	Source
Tensile strength	σ_c	(0.34 ± 0.06) MPa	3
Young's modulus	E	(410 ± 50) MPa	3
Poisson's ratio	ν	0.4	3 ^b
Linear contraction	$\alpha_T \Delta T$	$\frac{1}{3}$ 10%	3
Temperature front width	w	(4 ± 2) mm	3
Column diameter	ℓ	(2 ± 1) mm	3

^a The values are all taken from 3: this paper, section 2. The temperature front width w is from thermocouple measurements.

^b No measurements of the Poisson's ratio of stearic acid were found in the literature, and it was therefore estimated to be about $\nu = 0.4$ based on the Poisson's ratio of other hydrocarbon materials.

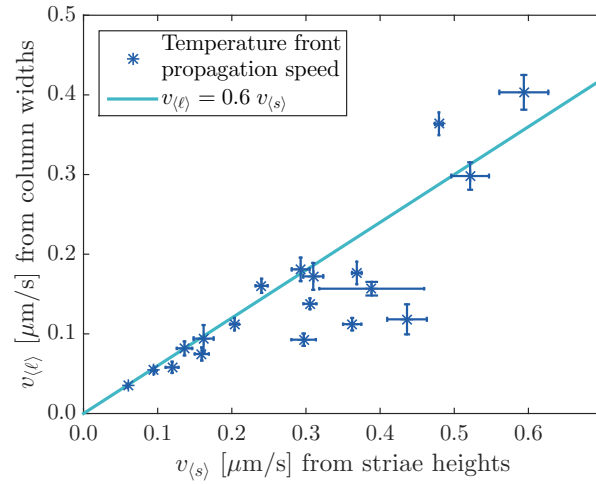


Figure 8. The temperature front propagation speed, $v = Pe D/\ell$, is estimated for different field locations using two different methods requiring different input measurements: column diameter, $\langle \ell \rangle$, and striae height, $\langle s \rangle$, respectively. The v -values on the y -axis are calculated using the scaling function $Pe = f^{-1}(\kappa_{I,c})$, and field measurements of the average column diameter, $\langle \ell \rangle$, from [Goehring and Morris, 2008]. The v -values on the x -axis are calculated on the basis of field measurements of striae heights, $\langle s \rangle$, at the same sites following [Goehring et al., 2009]. Each point represents one field location.

Table 3. Physical properties of basalt and parameters of the temperature front in the Columbia River Basalt Group^a

Property	Symbol	Value	Source
Fracture toughness	$K_{I,c}$	2.2 MPa $\sqrt{\text{m}}$	1
Young's modulus	E	50 GPa	5
Poisson's ratio	ν	0.2	5
Linear coefficient of thermal expansion	α_T	$7 \cdot 10^{-6}/^\circ\text{C}$	5
Thermal diffusivity	D	$6.5 \cdot 10^{-7} \text{ m}^2/\text{s}$	5
Max. temperature difference	ΔT	990°C	5

^a The values are taken from 1: *Degraff and Aydin* [1993] and 5: *Goehring and Morris* [2008]. The maximum temperature difference, ΔT , is calculated as the emplacement temperature minus 100°C, which is the temperature of the steam convection zone.

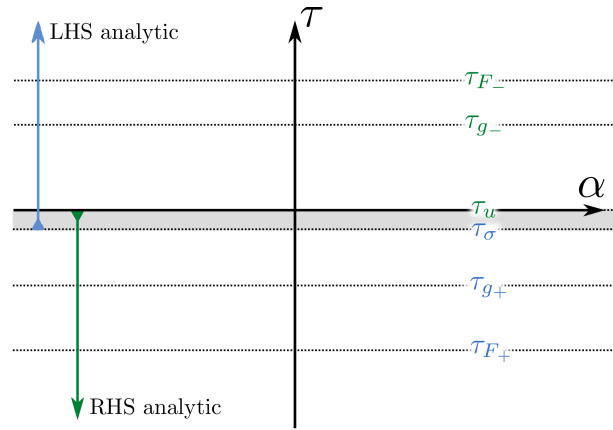


Figure 9. Regions of analyticity in the complex plane for different functions. The left hand side of Eq. (A20) is analytic in the region indicated by the blue arrow, whereas the right hand side of Eq. (A20) is analytic in the region indicated by the green arrow. The common strip of analyticity is gray shaded and covers the region $-\epsilon < \tau < 0$ in the complex plane $q = \alpha + i\tau$.

Table 4. Overview of the regions where the $+/-$ functions are analytical and non-zero. The zeros of $F(q)$ closest to the real axis were numerically determined to be at $\tau = \pm 2.1062$. Thus, the zeros occur closer to the real line than the first poles at $\tau = \pm\pi$, and the value of τ_{F-} and τ_{F+} are set by these zeros.

Upper half plane		Lower half plane	
τ_{σ}	$-\epsilon$	τ_u	0
τ_{h_+}	-2.1062	τ_{h_-}	0
τ_{F_+}	-2.1062	τ_{F_-}	2.1062
max τ	$-\epsilon$	min τ	0

Table 5. List of simulation parameters used in the discrete element simulations.

Simulation parameter	Value
Poisson's ratio	$\nu = 0.2$
Critical strain	$\epsilon_c \in [0.07, 2.60] \cdot 10^{-2}$
Maximal contraction	$\alpha_T \Delta T \in [0.01, 0.04]$
Dim.less. critical stress intensity factor ^a	$\kappa_{I,c} = \frac{\epsilon_c}{\alpha_T \Delta T}$
Temperature front width	$w \in [1, 24]$

^a In Figure 7 the value of $\kappa_{I,c}$ has been multiplied with $(1 - \nu)$ to make it comparable with the scaling function derived for 2D.

Table 6. List of simulation parameters used in the finite element simulations.

Simulation parameter	Value
Poisson's ratio	$\nu = 0.25$
Tensile strength	$\sigma_c = 0.01E$
Maximal contraction	$\alpha_T \Delta T = 0.02$
Dim.less. critical stress intensity factor ^a	$\kappa_{I,c} = \frac{\sigma_c}{E \alpha_T \Delta T} = 0.5$
Temperature front width	$w \in [1/18, 1/12]$

^a In Figure 7 the value of $\kappa_{I,c}$ has been multiplied with $(1 - \nu)$ to make it comparable with the scaling function derived for 2D.

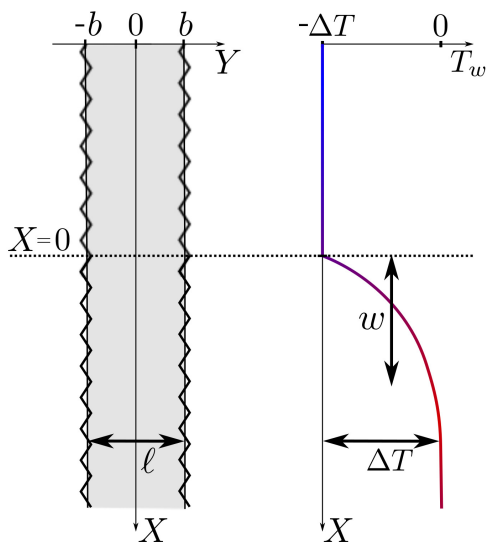


Figure 10. Example of the resulting fracture network in a finite element simulation of columnar jointing for $w = 1/15$ and the parameters displayed in Table 6.